ELSEVIER

PII S0730-725X(96)00113-5

● *Original Contribution*

A TECHNIQUE FOR SINGLE-CHANNEL MR BRAIN TISSUE SEGMENTATION: APPLICATION TO A PEDIATRIC SAMPLE

JAGATH C. RAJAPAKSE,* JAY N. GIEDD,* CHARLES DeCARLI,† JOHN W. SNELL,‡
ALAN McLAUGHLIN,§ YOLANDA C. VAUSS,* AMY L. KRAIN,*
SUSAN HAMBURGER* AND JUDITH L. RAPOPORT*

*Child Psychiatry Branch, National Institute of Mental Health, Building 10, Room 6N240, 10 Center Drive, MSC 1600,
Bethesda, MD, 20892-1600, †Epilepsy Research Branch, National Institute of Neurological Disorders and Strokes,
Bethesda, MD, ‡Department of Neurosurgery, University of Virginia, Charlottesville, VA,
§Clinical Brain Disorders Branch, National Institute of Mental Health, Bethesda, MD, USA

A segmentation method is presented for gray matter, white matter, and cerebrospinal fluid (*CSF*) in thin-sliced single-channel brain magnetic resonance (*MR*) scans. The method is based on probabilistic modeling of intensity distributions and on a region growing technique. Interrater and intrarater reliabilities for the method were high, and comparison with phantom studies and hand-traced results from an experienced rater indicated good validity. The method was designed to account for spatially dependent image intensity inhomogeneities. Segmentation of MR brain scans of 105 (*56 male and 49 female*) healthy children and adolescents showed that although the total brain volume was stable over age 4–18, white matter increased and gray matter decreased significantly. There were no sex differences in total gray and white matter growth after correction for total brain volume. White matter volume increased the most in superior and posterior regions and laterality effects were seen in hemisphere tissue volumes. These findings are consistent with other reports, and further validate the segmentation technique. 1996 Elsevier Science Inc.

Keywords: Magnetic resonance imaging; Brain imaging; White matter; Gray matter; Cerebrospinal fluid; Region growing.

INTRODUCTION

Magnetic resonance (*MR*) imaging, because of its lack of ionizing radiation, excellent spatial resolution, and ability to acquire images in any plane of orientation is an invaluable tool for in vivo anatomical studies. Classification of MR image voxels as gray matter, white matter, or cerebrospinal fluid (*CSF*) is important for brain anatomical research because these contrasts define the boundaries of most brain structures.[1,2]

The majority of automated tissue segmentation strategies have relied on multiple-channel image data in which information from nearly simultaneously acquired images highlighting different tissue characteristics, such as T_1 and T_2 relaxation times and proton density, are integrated to maximize discriminating power.[1,3–13] Because of the limitation of the clinically acceptable imaging times, pulse sequences giving geometrically registered multiple-channel data usually

yield images with large voxel sizes; a major drawback for multiple-channel techniques. A phantom study has shown that the error in volume computation and the effects of partial volume averaging rise as voxel size increases.[14] Large voxel sizes introduce significant partial voluming effects and do not provide adequate spatial resolution to accurately quantify small, but biologically important, subcortical structures. However, multi-channel data has more tissue discriminating power than single-channel data since multi-channel images provide more information at a voxel site from multiple images. Single-channel images do not provide multi-dimensionality of feature space, but typically yield smaller voxels and produce high contrast between gray and white matter. This article presents an automated method for gray and white matter segmentation for single-channel cerebral images.

Currently available methods for MR image segmentation can be categorized into classical, statistical,

Address correspondence to Dr. Rajapakse.

fuzzy, and neural network techniques.[15,16] Classical techniques include the use of standard image processing techniques such as thresholding,[17] edge-based,[18-20] and pixel-based[21,22] techniques. Although neural network techniques have been proposed for MR image segmentation, they have not been applied to large databases.[23,24] Fuzzy segmentation techniques are yet to be applied to single-channel image segmentation.[25,26]

Classical edge-based approaches extract tissue borders defined by intensity transitions or by gradients of intensity transitions and have been used to manually or semi-automatically outline cortical and subcortical structures.[18-20] These methods are slow and subject to user specific errors, and have not been successful due to random noise and the complex nature of the edge patterns in the brain images. In pixel-based methods, the intensity of a pixel gives the probability of the pixel being a member of a particular tissue. A threshold is usually defined based on the histogram of the image, and pixels with intensity above the threshold belong to a particular tissue while pixels with intensity values below the threshold belong to the other tissue. Pixel-based methods used in previous publications have been successful in segmenting CSF from brain parenchyma,[21] but have had only limited utility in segmenting gray and white matter from single-channel images.[22] Thresholding and clustering techniques for segmentation based on the histogram of the MR images do not work well because of the presence of random noise and magnetic field inhomogeneities.

Because thin-sliced single-channel images produce many slices per brain, an ideal segmentation method for large samples should be automated, fast, reliable, and valid. The method presented is automated and applicable to a larger database. The segmentation is statistical, "pixel based," and achieved through probabilistic modeling of gray and white matter distributions and a region growing technique. The method does not use a prior model such as a Markov random field as proposed by others,[27] because there is no systematic way of estimating the model parameters. To show the capability and usefulness of the present method, it was applied to segment 105 brain scans of healthy children and adolescents, aged 4–18, in our MR brain image data base. The segmented cerebrums were geometrically divided into 16 regions and the volumes of gray and white matter in these regions were computed to assess regional brain maturation across the understudied age range of 4–18 years.

Two groups of investigators,[5,28-32] have used multiple-channel thick MR slices and an optimal combination of proton-density and T_2 weighted images for discriminating gray and white matter and CSF in pediatric populations. Their techniques successfully segmented cortical gray and white matter, but were unable to seg-ment subcortical gray and white matter and, therefore, subcortical gray matter structures were outlined by hand-tracing.[31] The present method successfully segments both cortical and subcortical gray and white matter and the analysis contains regional subdivisions of cortical and subcortical brain regions. The smaller voxels in the present study may provide more accurate information, more sensitive to influences of region, gender, and age.

MATERIALS AND METHODS

Subjects

Healthy male ($n = 56$) and female ($n = 49$) children and adolescents were recruited from the community. Individuals with physical, neurological, or lifetime history of psychiatric abnormalities or who had first-degree relatives with major psychiatric disorders were excluded. Subject recruiting and screening, and brain structure measurements for these subjects are presented elsewhere.[33]

Hardware

All subjects were scanned on a GE 1.5 Tesla Signa scanner. Images with slice thickness of 1.5 mm in the axial plane were obtained using three-dimensional spoiled gradient recalled echo in the steady state (3D SPGR). Imaging parameters were TE = 5 ms, TR = 24 ms, flip angle = 45°, acquisition matrix = 192 × 256, number of repetitions = 1, and field of view = 24 cm. SPGR sequences are mainly sensitive to T_1 relaxation response times of the imaging tissues.

Preprocessing

Each SPGR axial image consisted of 124 slices of 16-bit images of size 256 × 256. The images were converted to 8-bit images before further processing, to speed up subsequent computations and reduce memory requirements. Images were then filtered with three-dimensional anisotropic filter (number of iterations = 4, $k = 10$, no bias) to improve signal-to-noise ratio and contrast-to-noise ratio of the images.[34,35]

Images of a representative brain slice, before and after filtering are shown with their histograms in Fig. 1. The filtering process smoothens out the regions without disturbing the regional boundaries. The histogram of an image indicates combined probability distributions of constituent tissue types. As seen in the figure, the filtering process reduces the variances of the intensities of tissues without altering the means of intensities. This enhances the segmentation of gray and white matter.

Brain shelling

The filtered images were transferred to a HP 9000/ 700 series workstation to run the brain shelling pro-
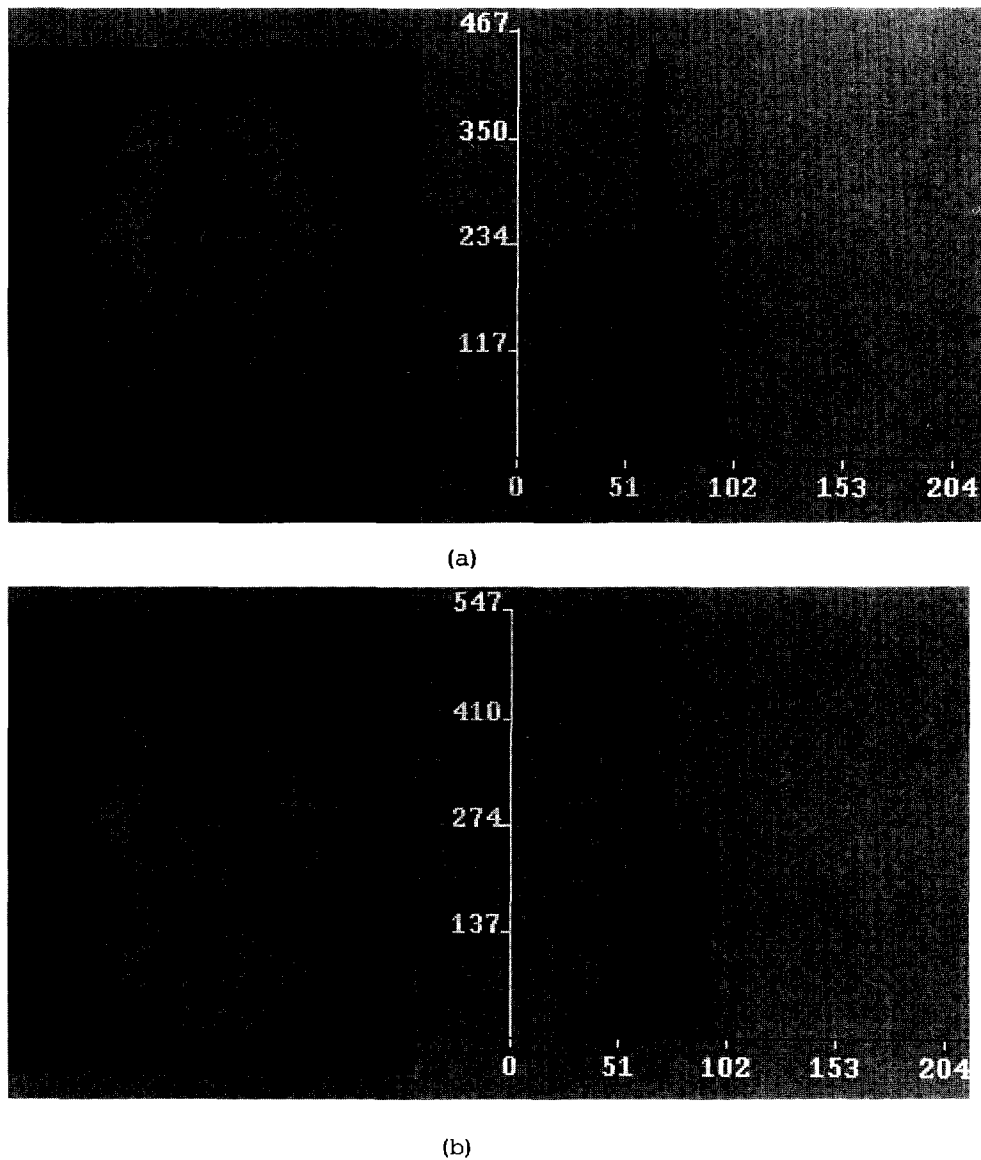
Fig. 1. SPGR image slices, and their pixel intensity histograms (a) before and (b) after anisotropic filtering.

gram, UvaSegmentor, developed by J.W.S. at the University of Virginia.[36] UvaSegmentor executes the brain shelling program based on an active brain surface template and separates left and right cerebrum and cerebellum from the head scans. Brain shelling refers to separation of cerebrum from external skull, bone, dura, brain stem, and cerebellum of the MR scans. A brain model composed of separate models of left and right cerebellum and cerebrum, which stores the a priori anatomical knowledge of the brain, is used in the shelling program.

When an input image is applied, the model is initiated within a stereotaxic coordinate framework.[37] The orientation of the coordinate system is defined by the interhemispheric fissure and the anterior and posterior commissures, which is done by adjusting user specified landmarks: anterior commissure; posterior commissure; and the most anterior, most posterior, most inferior, and most superior points of the cerebrum. A threshold of pixel intensities is also manually selected for foreground/background separation. This allows the model to coarsely register to the applied brain image. The model then deforms so as to satisfy the requirements of the extracted features of the given image using an energy minimizing function.[36] As the surface converges, the earlier selected threshold removes the background pixels and any CSF voxels that are below the threshold. The resulting surface effectively separates the cerebrum and cerebellum from the head scan. This method of brain shelling has been validated

against cadaver brains and further details are reported elsewhere.[36]

All shelled brains were then edited by experienced raters to remove artifacts related to patches of dura or eye ball not removed by UvaSegmentor. After shelling and editing, only gray and white matter are left, leaving the segmentation process to separate gray and white matter in the cerebrum. The ventricular CSF removed was quantified and used in the computation of total cerebral volume. The time required for shelling a single brain is about 20 min.

Gray and white matter segmentation

The segmentation was done slice by slice, one image slice at a time. Every image slice was assumed to be a rectangular array of $n \times m$ pixels where n and m are integers and the image intensity of a pixel at location $x \in A = \{(0,0),(0,1) \ldots (n,m)\}$ on a slice will be denoted by $I(x)$. We consider that the pixels are "pure" and contain only one type of tissue. Since CSF is not present in the shelled images, we model the intensity of an image slice with two tissue distributions: gray matter (G) and white matter (W) and assume probability distribution of intensities in each tissue to be Gaussian.

With Gaussian assumption, the probability of a pixel at location x being white matter, $p_W(x)$ can be written as:

$$p_W(x) = \frac{1}{\sqrt{2\pi\sigma_W^2(x)}} e^{-\frac{1}{2}\left(\frac{I(x)-\mu_W(x)}{\sigma_W(x)}\right)^2} \quad (1)$$

where $\mu_W(x)$ and $\sigma_W(x)$ are the mean and the standard deviation of the white matter intensity distribution at pixel location x, respectively. Similarly, the probability of the pixel at location x being gray matter, $p_G(x)$ can be written as:

$$p_G(x) = \frac{1}{\sqrt{2\pi\sigma_G^2(x)}} e^{-\frac{1}{2}\left(\frac{I(x)-\mu_G(x)}{\sigma_G(x)}\right)^2} \quad (2)$$

where $\mu_G(x)$ and $\sigma_G(x)$ are the mean value and the standard deviation of the gray matter intensity distribution at location x.

The algorithm calculates the probabilities of a pixel being a particular tissue type at each pixel location using Eqs. (1) and (2). The decision of whether a pixel is white matter or gray matter is taken according to the maximum likelihood (ML) criteria.[38] That is, the pixel at location x is decided to be gray matter if:

$$P_G(x) > p_W(x) \quad (3)$$

and it is decided to be white matter if:

$$P_W(x) > p_G(x) \quad (4)$$

otherwise, when the equality occurs, a new decision is not made. The program goes from one pixel to the other iteratively and makes decisions according to Eqs. (3) and (4).

To compute probabilities using Eqs. (1) and (2), one should know the parameters of the distributions. At the beginning of iterations, tissue parameters are initialized using those derived from the input image. If the average intensity of the image location x is $\mu(x)$ and standard deviation is $\sigma(x)$, the parameters of the distributions are initialized as follows:

$$\sigma_W(x) = \sigma_G(x) = K_1 . \sigma(x) \quad (5)$$

$$\mu_W(x) = \mu(x) + k_2 . \sigma(x) \quad (6)$$

$$\mu_G(x) = \mu(x) - k_2 . \sigma(x) \quad (7)$$

where k_1 and k_2 are two real positive constants and determine shapes and separation of the initial distributions. It was found that $k_1 = k_2 = 0.5$ worked well with our images. $\sigma(x)$ and $\mu(x)$ were calculated by considering a local neighborhood window D, about the location x. We used the size of $D = 25 \times 25$.

In the above Gaussian mixer model for brain parenchyma, the prior probabilities of the gray and white matter were assumed to be equal. When initializing the parameters, the two Gaussian distributions were placed at equal distances from and on the opposite sides of the mean intensity of the histogram. Further, the variances of gray and white matter intensities were made equal and proportional to the image variance. In the absence of any prior information, these assumptions worked well with our images.

As the classification proceeds, gray and white matter regions grow, and the parameters of the distributions are updated whenever a decision is made at a pixel, as the pixel characteristics change from one pixel to the other. If the decision at pixel location $\times$ is made to be white matter, then the parameters of the pixels within the neighborhood window D are updated as follows:

$$\mu_W(x + v) = \frac{n_W(x + v)\mu_W(x + v) + I(x)}{n_W(x + v) + 1} \quad (8)$$

$$\sigma^2_W(x + v) =$$
$$\frac{n_W(x + v) \cdot \sigma_W^2(x + v) + (\mu_W(x + v) - I(x))^2}{n_W(x + v) + 1} \quad (9)$$

$$n_W(x + v) = n_W(x + v) + 1 \quad (10)$$

where $v \in D$, and $n_W(x + v)$ is the total number of white matter pixels already classified as white matter about

location $x + v$. Similarly, when a pixel at location x is decided to be gray matter, the parameters of gray matter distributions at the neighborhood are updated as follows:

$$\mu_G(x + v) = \frac{n_G(x + v) \cdot \mu_G(x + v) + I(x)}{n_G(x + v) + 1} \quad (11)$$

$$\sigma_G^2(x + v) =$$
$$\frac{n_G(x + v) \cdot \sigma_G^2(x + v) + (\mu_G(x + v) - I(x))^2}{n_G(x + v) + 1} \quad (12)$$

$$n_G(x + v) = n_G(x + v) + 1 \quad (13)$$

where $v \epsilon D$, and $n_G(x + \nu)$ is the total number of gray matter pixels already classified as gray matter at location $x + v$.

The decision making process continued over the image slice several times until it became stable. The iterations were terminated when there were no changes in the decision making process. Usually, the decision making process became stabilized in three or four iterations. At the end of the iterations, the volumes of gray matter and white matter were stored separately and their regional volumes were measured.

The neighborhood window size D was determined using a trial and error technique. The optimal value of window size depends on the minimum structure needed to be segmented over the image. When the number of pixels belongs to a particular tissue within a neighborhood window D at a pixel site dropped below a threshold (the value 5 was used here), the tissue class at such a site was assigned to the other type of tissue.

The segmentation algorithm was implemented in a Unix/C environment and applied to MR scans of children and adolescents.

Application to mr images

All scans were interpreted by a neuroradiologist who found no evidence of tumors or tissue abnormalities. After CSF was removed by the shelling process, the remaining brain matter voxels were segmented into gray or white matter. Although the present method categorized blood vessels often as white matter and occasionally as gray matter, the percentage error resulted from vasculature was negligibly small.

Our methodology assumes "pure pixels" throughout the image, which in actuality, is not true at tissue boundaries since these voxels may contain a mixture of tissues. "Mixed pixels" can introduce partial volume effects, that is, statistical and misclassification errors, to the segmentation process. Partial volume effects at the gray and CSF boundaries occur with the shelling process and are determined at the thresholding step in

UvaSegmentor. The mixed pixels of CSF and gray matter left with the brain matter is subsequently classified as gray matter. Mixed pixels at the gray and white matter boundaries may introduce misclassification errors in the segmentation process. However, because the voxel size used here is smaller, the error due to partial volume effects is less than that from multiple-channel images.

Intensity of a voxel is statistically determined by the probability distribution of its tissue type over the image. Since the image intensity is generated by relaxation properties of brain cells and corrupted by random errors and noise of the scanner, the distributions were assumed to be Gaussian. Several probability maps generated using this assumption are shown in Fig. 2 to demonstrate the method and the effects of partial volume averaging. A probability map shows probability values of interest as the gray values of intensities at pixels. Figures 2a and 2b show probability maps of gray matter (i.e., each pixel intensity indicates the probability of being gray matter) and white matter, respectively, computed by the present algorithm over a brain slice. These maps show the ability of the method to classify gray and white matter in both cortical and subcortical regions. Maps in Figs. 2c and 2d indicate the maximums and the differences of probabilities of pixels being gray matter and white matter, respectively. At the gray and white matter boundaries, both probabilities were low indicating partial volume effects. The dark pixels in the maps are the pixels that are most likely to be misclassified as even a small difference leads to segmentation of pixels since the classification is determined by the maximum likelihood criteria.

Even with high quality MR imaging scanner, region dependent variations of intensities are present over the images due to irregularities of the field strength and the sensitivity of the receiver coil.[39] This has been a major obstacle for intensity-based MR image segmentation methods. Inhomogeneities in the images change the parameters of the intensity distributions spatially and for this reason, the parameters of the intensity distributions were evaluated locally at each point. This procedure accounts for spatial variations of the intensities over the image as inhomogeneities are usually smoothly varying and the tissue intensities may not vary over a small neighborhood.[40] Calculation of parameters at each pixel location considering neighborhood pixels is computationally intensive and slows down the segmentation process. If the images are free from inhomogeneities, a fast version (global version) of the algorithm can be used, where a single set of parameters is evaluated over the image slice.

Definition of cortical and subcortical regions

Anatomical boundaries of the cortex often depend on gyral and sulcal patterns, quantification of which is beyond our current methodology. Therefore, as a crude

(a)   (b)

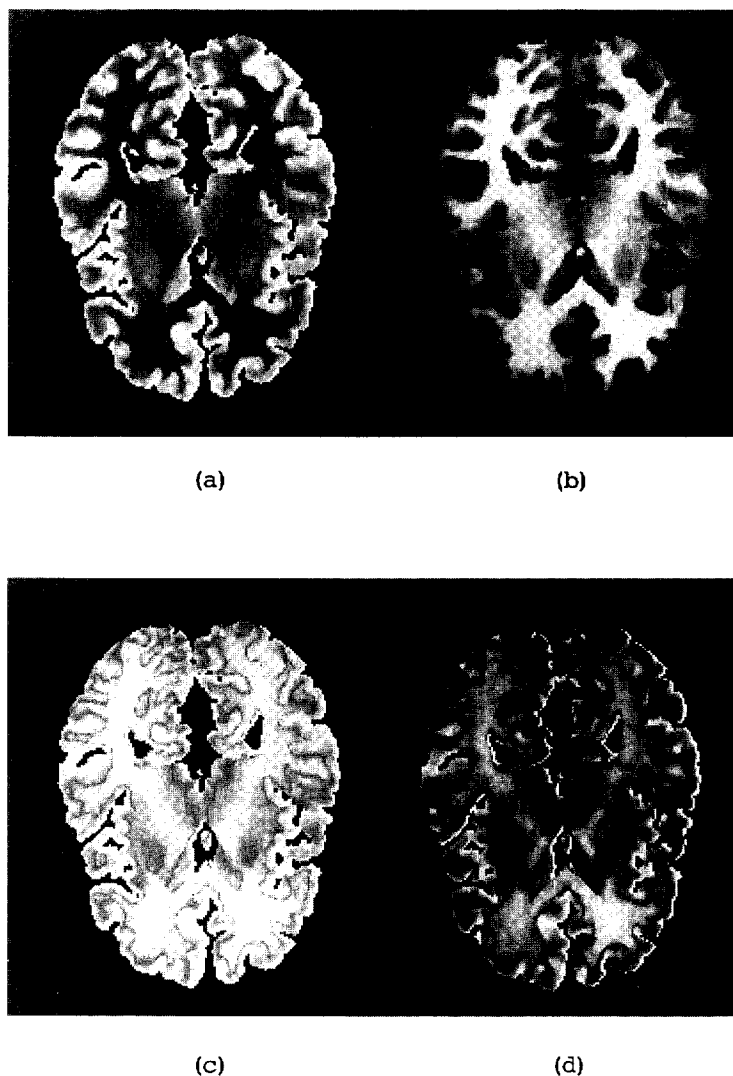
(c)   (d)

Fig. 2. Probability maps with pixel intensity indicating the likelihood of a given pixel being (a) gray matter and (b) white matter. Illustration of correct classification of tissue categories using (c) maximum of gray and white matter probabilities and (d) the differences of gray and white matter probabilities.

regional evaluation of the segmented tissue volumes, the cerebrum was divided geometrically into 16 subregions. Cortical and subcortical division was defined using the method adopted by Pfefferbaum et al.,[31,32] in which cortical region consisted of the outer 45% of the brain, and was established anatomically by concentrically stripping a rim of voxels from the periphery of the brain, until 45% of the brain voxels were removed. The inner 55% constituted the subcortical region.

To ensure some anatomic consistency of cerebral regions, the cerebrum was subdivided relative to two subcortical landmarks, the anterior commissure (AC), and posterior commissure (PC). The AC point on the plane of the interhemispheric fissure (midline plane) is a major landmark of the brain that remains constant with age.[37] A coronal plane (AC plane) was drawn perpendicular to

the midline plane at the AC point, defining the boundary between anterior, and posterior regions.

To standardize the head placement and define a reference plane for our images, before scanning, vitamin E capsules had been placed in the auditory meatus of each subject's ears and on the lateral aspect of the left inferior orbital ridge. Even with these attempts to standardize the head placement, however, rotation of the brain image in all three axis may occur due to subtle movements of the head, changing the placement and appearance of the images. Therefore, before processing, all head scans were rotated in three-dimensional space and aligned so that AC and PC points were on the same axial plane (AC-PC plane) and the plane passing through the midline was perpendicular to the AC-PC plane. This was done by locally written

software with location of AC and PC points and two points on the midline taken as inputs. The voxels above and below the AC-PC plane are referred to as superior and inferior, respectively.

The resulting 16 regions (left and right hemispheres, with anterior-posterior, superior-inferior, and cortical-subcortical subdivisions) are shown in Fig. 3, and similar to those used by Jernigan et al.[30]

RESULTS

Interrater and intrarater reliabilities

Since gray and white matter segmentation is fully automated, the reliability of the present segmentation method mainly depends on the brain shelling process whose consistency and accuracy depends on the selection of the landmarks to initiate the brain model in stereotaxic coordinate framework, and the threshold for foreground/background differentiation.

To obtain the intrarater reliability, 10 brains were selected and each brain was filtered, shelled and segmented for gray and white matter twice by an operator (Y.C.V.). The intrarater correlation coefficients (ICC) were calculated for the two attempts and ICC values for gray matter, white matter, and total brain volume were 0.995, 0.996, and 0.995, respectively. Interrater reliability, was also determined between two of our raters with segmentation of 10 brains and the ICC values were 0.980, 0.915, and 0.950 for gray matter, white matter, and total brain volume, respectively.

Phantom studies

Any phantom used to validate the method should mimic the characteristics of gray and white matter and simulate the problems encountered in the segmentation process. A large variety of materials are available for making phantoms that mimic tissue parameters.[41] Based on previous reports,[42] various concentrations of dextran-coated superparamagnetic iron oxide particles (AMI-25 particles, Advanced Magnetics) in agarose gel (Sigma Chemical Co. Type 1, Low EEO) were selected to model the relaxation properties of the tissue types.

Addition of iron oxide particles decreased T_1 relaxation time of the gel resulting in an increase of image intensity[42] in the partially saturated imaging parameters used for this study. Initially, test-tube phantoms of 1% (wt/vol) agarose with various concentration of iron oxide (0–50 μMolar) were investigated. By comparing the intensities with the actual tissue intensities, iron oxide concentrations for gray and white matter were determined. Concentrations of 33 μMolar and 6.7 μMolar of iron oxide were selected to represent white and gray matter, respectively, and a phantom was constructed with agarose gel in a cylindrical plastic bottle. Initially, gel with 33 μMolar of iron concentration was melted and poured into the bottle, and then once it was hardened, molten gel with 6.7 μMolar iron concentration was poured. This simple phantom was chosen because our segmentation method is "pixel based" and does not take shape into account. Although partial volume effects depend on the shape of the phantom, the small voxel size used here minimizes these effects.

The phantom was imaged parallel to the long axis, in the same manner as our subjects. The phantom image was then segmented and volumes of gray and white matter were measured. Figure 4 shows an image slice of the phantom and the results of segmentation. Table 1 shows

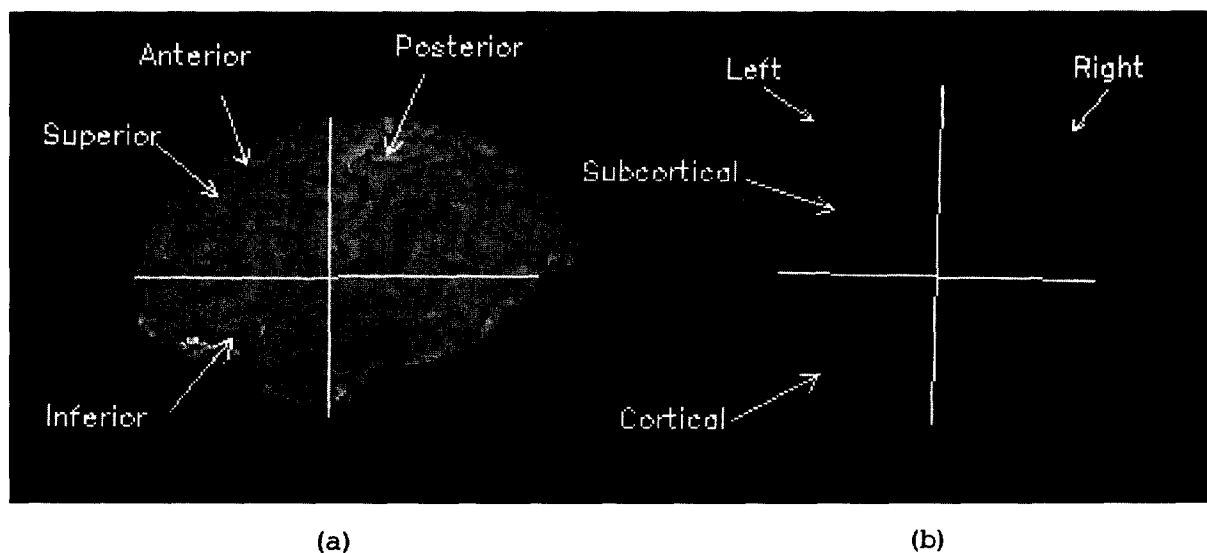(a)   (b)

Fig. 3. Illustration of regional subdivisions of the brain. (a) Anterior and posterior, and inferior and superior divisions shown on a lateral view of the brain. (b) Cortical and subcortical, and left and right divisions on an axial slice.
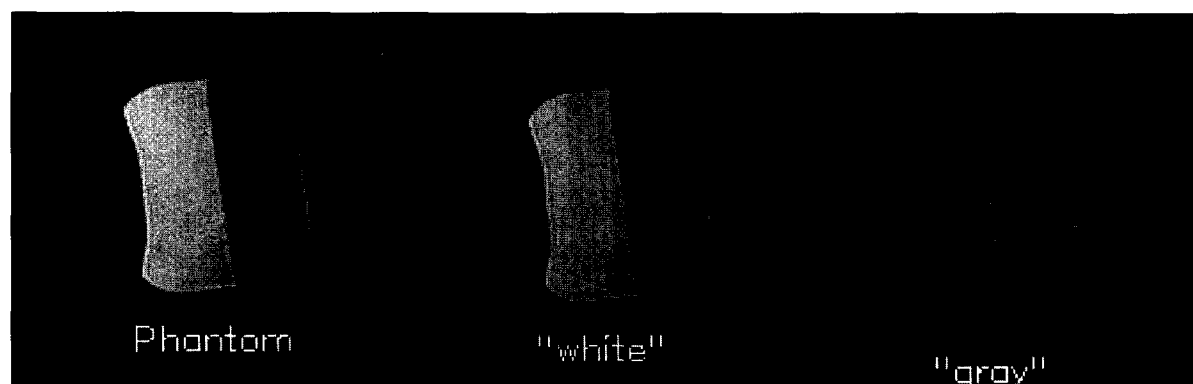
Fig. 4. Separation of gray and white matter of the phantom using the local version of the algorithm.

actual and measured volumes of the simulated tissues and errors resulting from segmentation using two versions of the algorithm: one with the global version where one set of parameters for the distributions were computed over the whole image, and the local version which was described above (see Materials and Methods). The local version of the algorithm gave more accurate results since it accounted for the presence of intensity inhomogeneities. The sum of the gray and white matter volumes segmented were slightly offset from 400 ml because of the error due to the bottle thickness.

Validation with manual-segmentation

Segmentation results were also compared with hand-segmented images by one of the authors with extensive experience in MR brain imaging (J.N.G.). Since hand segmentation is tedious and time-consuming process, the segmentation was done only on five slices of a brain image, taken from different parts of the brain, representing the whole cerebrum (i.e., a high cortex slice, a mid-ventricle slice, a slice at the basal ganglia region, a lower cortex slice, and a slice at medial temporal level). The same slices were also segmented using the segmentation algorithm. The brain image was again filtered and shelled, and the same slices were segmented by the same operator and by the algorithm, separately. The results of the two attempts and between manual and automated segmenta-

tion were compared in Table 2. Figure 5 shows the segmentation of three slices performed by the algorithm. The shelled image slices, segmented white matter and gray matter are shown in the columns, respectively, in the figure.

Except in the segmentation of the mid-ventricular slice, the differences between the hand and automated segmentation volumes were less than 10% of the total tissue volumes. Between the two attempts of manual segmentation of mid-ventricular slice, the error was more than 10%. This indicates that the complex boundaries of gray and white matter make manual segmentation of brain slices difficult and inconsistent. Still, subjective assessment by an experienced anatomist remains the best way to evaluate the output of a segmentation algorithm.[15] Even with extreme care, the segmentation using manual tracing showed a poor segmentation visually, compared to the segmentation produced by the algorithm. The results of the two attempts for the overall segmentation process using the algorithm were slightly offset due to the subjective determination of landmarks and the threshold during shelling.

Pediatric MR images

The segmentation algorithm was applied to 105 scans (56 males and 49 females) of shelled brains of children and adolescents. Significant sex differences

Table 1. Actual and measured volumes of different regions of the phantom

Sample region	Actual volume (ml)	Measured volumes (ml)		Differences	
		Global method	Local method	Global method	Local method
White	200.0	199.0	199.5	0.50%	0.25%
Gray	200.0	201.8	201.3	0.90%	0.75%

The different regions were composed of 1% agar gel with varying concentration of dextran coated iron oxide particles. The total iron concentration in the different regions were: "white matter", 33 μM; "gray matter", 6.7 μM. Measured volumes and the differences are shown for both local and global version of the algorithm.

Table 2. Validation of gray matter and white matter volumes obtained by the segmentation method against hand-tracing

Slice Level	Gray matter			White matter		
	Manual trace	Algorithm	Difference	Manual trace	Algorithm	Difference
High cortex:						
1st Attempt	3.966	4.203	−5.6%	5.905	5.668	4.0%
2nd Attempt	3.996	4.181	−4.6%	5.905	5.720	3.1%
Difference	0.0%	0.5%		0.0%	0.9%	
Mid-ventricular:						
1st Attempt	8.497	8.232	3.1%	10.358	10.623	−2.6%
2nd Attempt	7.020	8.266	−17.7%	11.835	10.589	10.5%
Difference	19.0%	−0.4%		−13.3%	0.3%	
Basal ganglia:						
1st Attempt	11.462	12.029	−4.9%	13.686	13.119	4.1%
2nd Attempt	11.392	11.791	−3.5%	13.756	13.357	2.9%
Difference	0.6%	2.0%		−0.5%	1.8%	
Lower cortex:						
1st Attempt	11.803	12.029	−1.9%	14.291	13.257	7.2%
2nd Attempt	12.444	12.245	1.6%	13.650	13.849	−1.5%
Difference	−5.3%	−1.7%		4.6%	−4.3%	
Medial temporal:						
1st Attempt	10.145	9.468	6.7%	10.002	10.679	−6.7%
2nd Attempt	9.690	9.550	1.4%	10.457	10.597	−1.3%
Difference	4.6%	0.9%		−4.4%	1.0%	

The volumes are in cubic centimeters, and the percentage difference = ratio of (hand-tracing−algorithm)/hand-tracing. The brain was filtered and shelled and each slice was hand-traced and segmented twice. The differences as the percentage of mean values of the two attempts are also shown.

for total cerebral volume ($p < .001$) were found with male brains 8.5% larger than the female brains, as previously reported for a subset of this sample.[33] There was no significant age-related increase of total cerebral volume across ages 4–18 ($p = .16$).

Regression analyses were carried out for total gray and white volumes with age. Since cerebral volume depends on the gender, the tissue volumes were divided by the total brain volume to remove the total brain volume effect. The regression lines are shown in Fig. 6. For both males and females, white matter volume increased significantly ($p < .001$) and gray matter volumes decreased significantly ($p < .001$). There were no significant differences between the male and female regression lines.

Multiple regression analyses were also done for regional gray and white matter volumes in relation to regional total volume and age. The posterior and superior regions showed the most robust changes with the age in both left-right, and cortical-subcortical regions. Across ages 4 to 18, the gray matter in these regions significantly decreased ($p < .001$) and white matter significantly increased ($p < .001$). This pattern of changes also appeared in the left anterior superior region of the brain while only trends were seen in anterior inferior cortical regions ($p = .56$ and .082 for gray and white matter, respectively). In addition, similar changes were seen in the left side of the posterior

inferior regions. Figure 7a illustrates the white matter variation in anterior and posterior regions with age, and Fig. 7b shows the variation of inferior and superior white volume change. The speeds of growth of white matter in the two regions in both cases differed significantly from each other.

ANOVA and ANCOVA were performed to test the laterality effects of tissue volumes. The left hemisphere had more white matter (in males 20.6 ml more and in females 14.6 ml more) and less gray matter (in males 10.2 ml less and females 4.3 ml less) than the right hemisphere.

DISCUSSION

An automated method for gray and white matter segmentation of single-channel MR brain scans is presented that appears valid and reliable and can be used to segment large data sets. Previous methods were semi-automated and designed for only multiple-channel MR brain scans with less than 20 slices representing a brain.[29-32] The present automatic method fills a need for analyzing MR image data sets with thin slices and more than 100 slices for each brain. The segmentation process took about 20 min per brain on our Sparc 10 workstation. Fortunately, the automated nature of the segmentation procedure allows several hundred brains to be processed as one batch. Although the con-

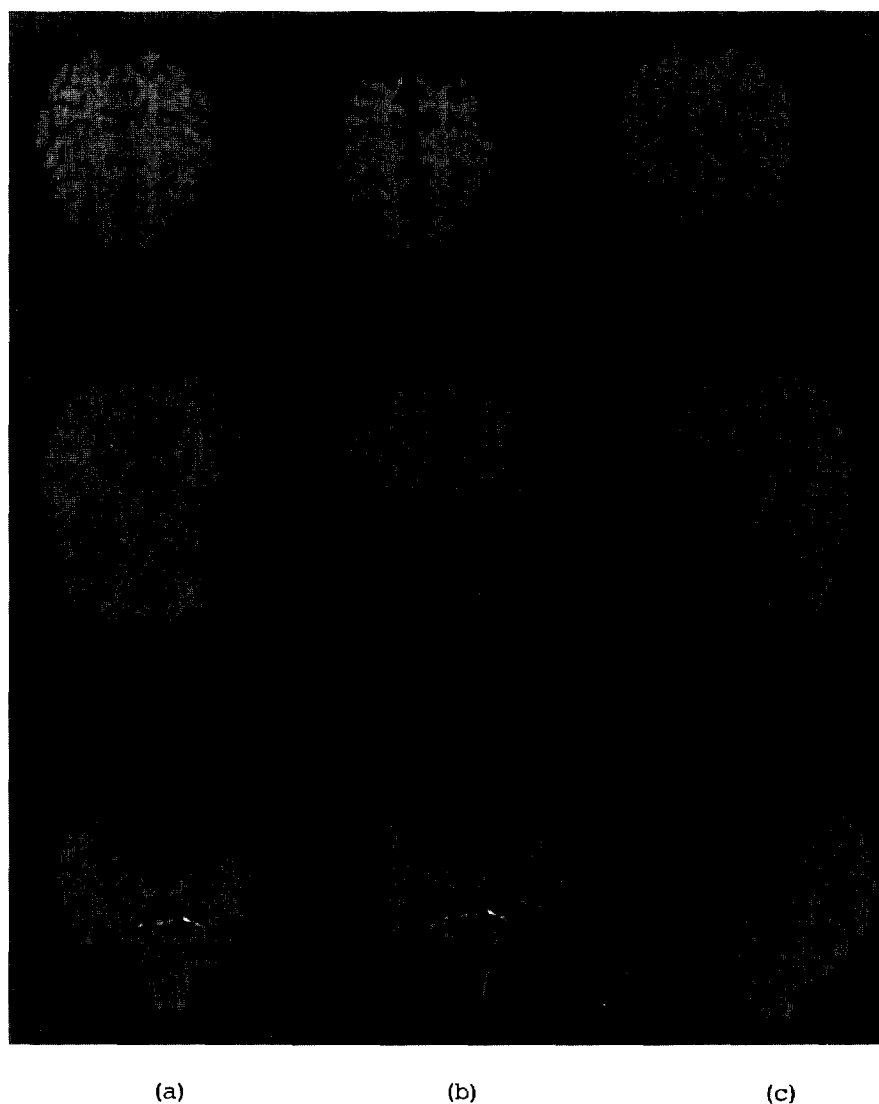(a)   (b)   (c)

Fig. 5. Illustration of gray and white matter segmentation of three slices of a brain image using the automated algorithm. (a) Shelled brain slice with CSF and skull excluded; (b) segmented white matter; and (c) gray matter.

vergence of the segmentation is achieved for all the brains tested, the convergence of the algorithm needs to be investigated.

Noise and random errors in the images were removed using anisotropic filtering, which improved noise and contrast without blurring edges or structural details,[34,35] while locally dependent parameters of the probability distributions overcame smoothly varying inhomogeneities of the intensities over the image. In addition, because slice by slice segmentation was adopted, the intensity variations in axial directions did not affect the segmentation scheme. As a result, it was not necessary to use any filter or other method for correcting inhomogeneities as the segmented images did not show any such effects. The phantom studies also confirmed greater accuracy for the local version

of the algorithm described here than with the global method, supporting the ability of the present algorithm to take inhomogeneities into account.

The present method accurately segments subcortical white and gray matter, which was not possible using previous methods utilizing multiple-channel MR data.[29-31] Subcortical gray matter was previously separated by hand-tracing,[31] which was prone to the variability due to subjective determination of tissue boundaries. Nevertheless, the present data supports the previous findings of decreasing subcortical gray matter across our age span.[31,33]

A disadvantage of our method is that CSF could not be quantified as ventricular CSF and sulcal CSF as it was removed during brain shelling. This did not permit us to find the relation between the variation of

Gray and White Matter Volume in Relation to Age in 105 Healthy Children and Adolescents

Gray Volume Vs. Age

White Volume Vs. Age

o ___ males y=0.400+0.004x, p<.001
◊ ... females y=0.401+0.003x, p<.001

o ___ males y=0.585-0.004x, p<.001
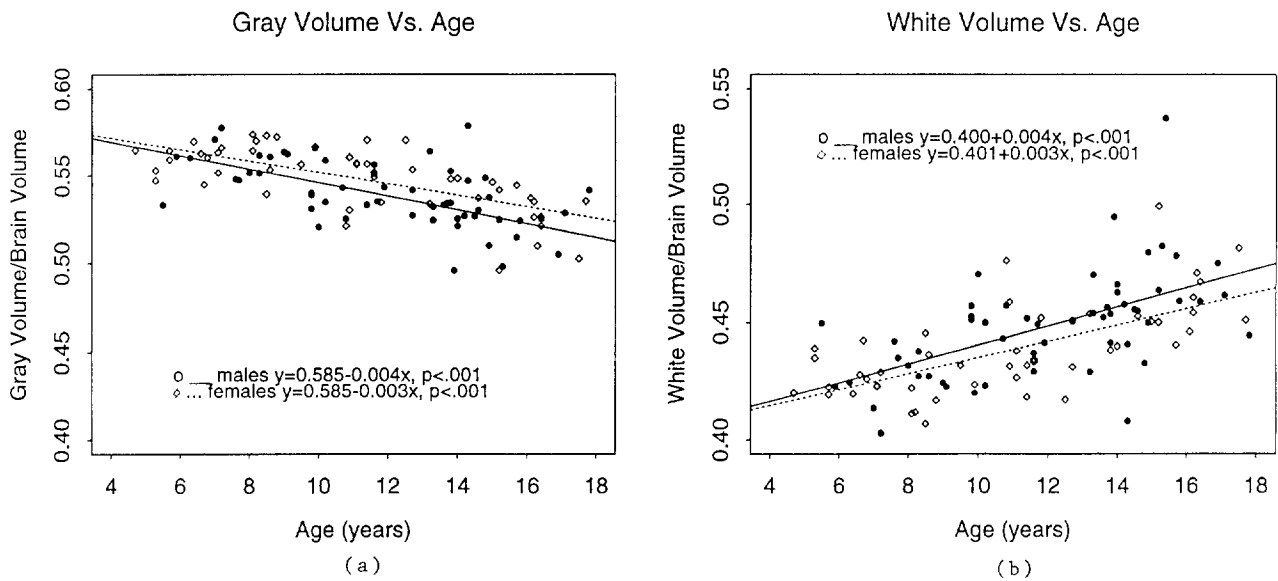◊ ... females y=0.585-0.003x, p<.001

(a)

(b)

Fig. 6. Scatter plots by age and gender of (a) gray matter volume/total brain volume; and (b) white matter volume/total brain volume for 105 children and adolescents.

CSF volume and the changes in volumes of the other tissues as others have done.[31] Although the partial volume effects are less with images with smaller voxel sizes, their presence at the tissue boundaries were seen with probability maps. Another disadvantage of our

method is that the regional subdivisions could not be related to sulcal and gyral patterns. Although functionally relevant regions based on sulcal and gyral patterns have been proposed,[43] implementation of an automated measurement technique to get regional volumes is dif-

Regional White Matter Volume Vs. Age for 105 Children and Adolescents

Anterior and Posterior White Volume Vs. Age

o ___ Anterior White, y=151.6+1.7x, p<0.001
◊ .... Posterior White, y=274.0+4.75x, p<0.001

Inferior and Superior White Volume Vs. Age

o ___ Inferior White, y=106.1+0.2x, p=0.742
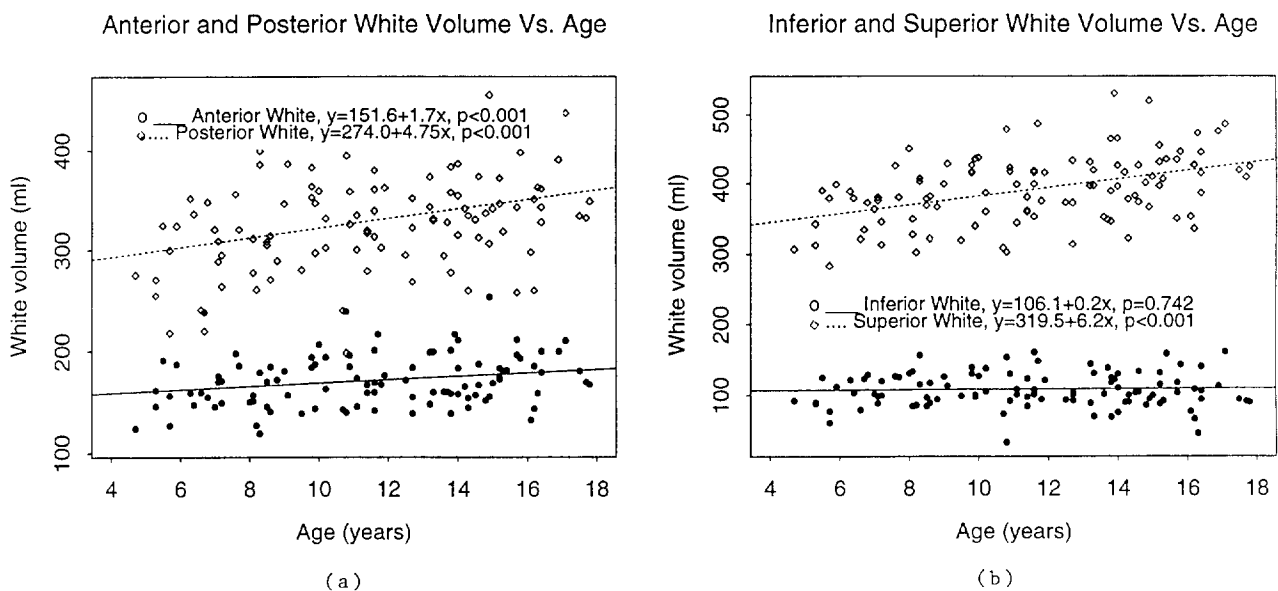◊ .... Superior White, y=319.5+6.2x, p<0.001

(a)

(b)

Fig. 7. Scatter plots by age and region of white matter volume for (a) anterior and posterior regions; and (b) inferior and superior regions for 105 children and adolescents.

ficult. The scatter seen in some of the measured regional tissue volumes could be due to arbitrariness in the definition of regional volume boundaries.

Age-related increase in white matter and decrease in gray matter are consistent with previous reports.[30,32] These changes are similar for males and females. The white matter increase demonstrates continuing myelination and axonal growth while the gray matter decrease presumably evinces cell death and synaptic pruning. White matter increase is seen mostly in superior regions and appears to be more rapid in the posterior segment. Posterior superior regions contain sensory integrational and associational areas while anterior superior regions involve higher cognitive functions,[44] and it is of interest that both of these regions showed significant growth in white matter across our age span, possibly reflecting brain maturation underlining developments of higher order cognitive and associational capacities.

Our technique of segmentation may be useful in measurement of brain tissues and in finding correlation of those measurements to behavioral and physiological parameters for clinical populations. Its application to the study of brain development in children and adolescents has been demonstrated, and the consistency of the results with earlier reports, further supports the validity of this technique. With thinner slices of single-channel data, higher accuracy of the measurements and less partial volume effects can be expected. The method is insensitive to nonhomogeneities over the image. These characteristics make it ideal for application to a large population of brain scans. Currently, the method is being used to segment brain scans of large samples of children with various neuropsychiatric disorders having onset in this understudied age period.

REFERENCES

1. Rajapakse, J.C.; DeCarli, C.; Giedd, J.N.; McLaughlin, A.; Hamburger, S.D.; Rapoport, J.L. Cerebral magnetic resonance image segmentation using data fusion. J. Comput. Assist. Tomogr. 20(2):208–216; 1996.

2. Yakovlev, P.I.; Lecours, A.R. The myelogenetic cycles of regional maturation of the brain. In: A. Minowski (Ed). Regional Development in Brain in Early Life. Oxford: Blackwell Scientific; 1967: pp. 3–69.

3. Cohen, G.; Andreasen, N.C.; Alliger, R.; Arndt, S.; Kuan, J.; Yuh, W.T.C.,; Ehrhardt, J. Segmentation techniques for the classification of brain tissue using magnetic resonance imaging. Psychiatry Res. 45:33–51; 1992.

4. Jernigan, T.L.; Press, G.A.; Hesselink, J.R. Methods for measuring brain morphologic features on magnetic resonance images: validation and normal aging. Arch. Neurology 47:27–32; 1990.

5. Lim, K.O.; Pfefferbaum, A. Segmentation of MR brain images into cerebrospinal fluid spaces, white and gray matter. J. Comput. Assist. Tomogr. 13(4):588–593; 1989.

6. Harris, G.J.; Barta, P.E.; Peng, L.W.; Lee, S.; Brellschnder, P.D.; Shah, A.; Henderer, J.D.; Schlaepfer, T.E.; Pearlson, G.D. MR volume segmentation of gray matter and white matter using manual thresholding: dependence on image brightness. Am. J. Neuroradiol. 15:225–230; 1994.

7. Harris, G.J.; Rhew, E.H.; Noga, T.; Pearison, G.D. User-friendly method for rapid brain and CSF volume calculation using transaxial MR images. Psychiatry Res. 40:61–68; 1991.

8. Raya, S.P. Low-level segmentation of 3-D magnetic resonance brain images—a rule-based system. IEEE Trans. Med. Imag. 9(3):327–337; 1990.

9. Vannier, M.W.; Butterfield, R.L.; Jordan, D.; Murphy, W.A.; Levitt, R.G.; Gado, M. Multispectral analysis of magnetic resonance images. Radiology 154:221–224; 1985.

10. Vannier, M.W.; Pilgram, T.K.; Speidel, T.M.; Neumann, R.L.; Rickman, D.L.; L.D. Schertz. Validation of magnetic resonance imaging multispectral tissue classification. Comput. Med. Imaging Graph. 15(4): 217–223; 1991.

11. Clarke, L.P.; Velthuizen, R.P.; Phuphanich, S.; Schellenberg, J.D.; Arrington, J.A.; Silbiger, M. MRI: stability of three supervised segmentation techniques. Magn. Reson. Imaging 11:95–106; 1993.

12. Liang, Z. Tissue classification and segmentation of MR images. IEEE Eng. Med. Biol. 39:81–85; 1993.

13. Choi, H.S.; Haynor, D.R.; Kim, Y. Partial volume tissue classification of multichannel magnetic resonance images. IEEE Trans. Med. Imaging 10(3)395–407; 1991.

14. Caviness, V.S.; Filipek, P.A.; Kennedy, D.N. Magnetic resonance technology in human brain science: blueprint for a program based upon morphometry. Brain Dev. 11(1):1–11; 1989.

15. Pal, N.R.; Pal, S.K. A review on image segmentation techniques. Pattern Recogn. 26(9):1277–1294; 1993.

16. Morrison, M.; Attikiouzel, Y. An introduction to the segmentation of magnetic resonance medical images. Aust. Comput. J. 26(3):90–98; 1994.

17. Sahoo, P.K.; Soltani, S.; Wong, A.K.C. A survey of thresholding technique. Comput. Vision Graph. Image Proc. 41:233–260; 1988.

18. Kennedy, D.N.; Filipek, P.A.; Caviness, V.S., Jr. Anatomic segmentation and volumetric calculations in nuclear magnetic resonance imaging. IEEE Tran. Med. Imag. 8(1):1–7; 1989.

19. Filipek, P.A.; Kennedy, D.N.; Caviness, V.S., Jr.; Rossnick, S.L.; Spraggins, T.A.; Starewics, P.M. Magnetic resonance imaging-based brain morphometry: development and application to normal subjects. Ann. Neurol. 25(1):61–67; 1989.

20. Filipek, P.A.; Richelme, C.; Kennedy, D.N.; Caviness, V.S., Jr. The young adult human brain: an MRI-based morphometric analysis. Cerebral Cortex 4(4):344–360; 1994.

21. DeCarli, C.; Maisog, J.; Murphy, D.G.M.; Teichberg, D.; Rapoport, S.I.; Horwitz, B. Method for quantifica-

tion of brain, ventricular and subarachnoid CSF volumes from MR images. J. Comput. Assist. Tomogr. 16(2): 274–284; 1992.

22. Van Meter, J.W. Segmentation and restoration of magnetic resonance images using material mixture models. Ph.D. Dissertation, Dartmouth College, September 1993.

23. Amartur, S.C.; Piraino, D.; Takefuji, Y. Optimization neural networks for the segmentation of magnetic resonance images. IEEE Tran. Med. Imaging 11(2):215–220; 1992.

24. Ozkan, M.; Dawant, B.M.; Maciunas, R.J. Neural network-based segmentation of multi-modal medical images: a comparative and prospective study. IEEE Tran. Med. Imaging 12(3):553–554; 1993.

25. Hall, L.O.; Bensaid, A.M.; Clarke, L.P.; Velthuizen, M.S.; Silbiger, M.S.; Bezdek, J.C. A comparison of neural network and fuzzy clustering techniques in segmenting magnetic resonance images of the brain. IEEE Tran. Neural Networks 3(5):672–682; 1992.

26. Brandt, M.E.; Bohan, T.P.; Kramer, L.A.; Fletcher, J.M. Estimation of CSF, white, and gray matter volumes in hydrocephalic children using fuzzy clustering of MR images. Comput. Med. Imaging Graph. 18(1):25–34; 1994.

27. Pappas, T.N. An adaptive clustering algorithm for image segmentation. IEEE Tran. Signal Proc. 40(4):901–914; 1992.

28. Jernigan, T.L.; Tallal, P. Late childhood changes in brain morphology observable with MRI. Dev. Med. Child Neurol. 32(5–6):379–385; 1990.

29. Jernigan, T.L.; Archibald, S.L.; Berhow, M.T.; Sowell, E.R.; Foster, D.S.; Hesselink, J.R. Cerebral structure on MRI, Part 1: localization of age-related changes. Biol. Psychiatry 29:55–67; 1991.

30. Jernigan, T.L.; Trauner, D.A.; Hesselink, J.R.; Tallal, P.A. Maturation of human cerebrum observed in vivo during adolescence. Brain 114:2037–2049; 1991.

31. Lim, K.O.; Zipursky, R.B.; Watts, M.C.; Pfefferbaum, A. Decreased gray matter in normal aging: an in vivo magnetic resonance study. J. Gerontol. 47(1):B26–30; 1992.

32. Pfefferbaum, A.; Mathalon, D.H.; Sullivan, E.V.; Rawles, J.M.; Zipursky, R.B.; Lim, K.O. A quantitative magnetic resonances imaging study of changes in brain morphology from infancy to late adulthood. Arch. Neurol. 51:874–887; 1994.

33. Giedd, J.N.; Snell, J.W.; Lange, N.; Rajapakse, J.C.; Kozuch, P.; Casey, B.J.; Kaysen, D.; King, A.C.; Hamburger, S.D.; Rapoport, J.L. Quantitative magnetic resonance imaging of human brain development: ages 5–18. Cerebral Cortex 6:551–560, 1996.

34. Perona, P.; Malik, J. Scale space and edge detection using anisotropic diffusion. IEEE Tran. Pattern Analy. Machine Intell. 12(7):629–639; 1990.

35. Gerig, G.; Kubler, O.; Kikinis, R.; Jolesz, F.A. Nonlinear anisotropic filtering of MRI data. IEEE Tran. Med. Imaging 11(2):221–232; 1992.

36. Snell, J.W.; Merickel, M.; Ortega, J.; Goble, J.; Brookeman, J.; Kassell, N. Model-based boundary estimation of complex objects using hierarchical active surface templates. Pattern Recognition 28(10):1599–1609; 1995.

37. Talairach, J.; Tournoux, P. (Eds). Co-Planar Stereotaxic Atlas of the Human Brain. New York: Thieme Medical Publishers, Inc.; 1988.

38. Duda, R.O.; Hart, P.R. Pattern Classification and Scene Analysis. New York: John Willey and Sons; 1973.

39. Chang, H.; Fitzpatrick, J.M. A technique for accurate magnetic resonance imaging in the presence of field inhomogeneities. IEEE Tran. Med. Imaging 31(3):319–329; 1992.

40. DeCarli, C.; Murphy, D.G.M.; Teichberg, D.; Campbell, G.; Sobering, G.S. Local histogram correction of MRI spatially dependent image pixel intensity nonuniformity. JMRI 6:519–528; 1996.

41. Madsen, E.L.; Fullerton, G.D. Prospective tissue-mimicking materials for use in NMR imaging phantoms. Magn. Reson. Imaging 1:135–141; 1982.

42. Bulte, J.W.; Douglas, T.; Mann, S.; Grankel, R.B.; Moskowitz, B.M.; Brooks, R.A.; Baumgarner, C.D.; Vymazal, J.; Strub, M.; Frank, J.A. Magnetoferritin: characterization of a novel superparamagnetic MR contrast agent. Magn. Reson. Imaging 4:497–505; 1994.

43. Rademache, J.; Galaburda, A.M.; Kennedy, D.N.; Filipek, P.A.; Caviness, V.S. Human cerebral cortex: localization, parcellation, and morphometry with magnetic resonance imaging. J. Cognitive Neurosci. 4(4):352–374; 1992.

44. Goldman-Rakic, P.S. The frontal lobes: uncharted provinces of the brain. Trends Neurosci. 7:425–429; 1984.